

I. Nomenclature

<i>APS</i>	= Air-Plasma Spray
<i>CFL</i>	= Courant-Friedrichs-Lowy Condition
<i>CMAS</i>	= Calcium-Magnesium-Alumino-Silicate
<i>EB – PVD</i>	= Electron Beam Particle Physical Vapor Deposition
<i>GCI</i>	= Grid Convergence Index
<i>GRD</i>	= Giordano (CMAS viscosity model)
<i>HRIC</i>	= High-resolution Interface Capturing
<i>TBC</i>	= Thermal Barrier Coating
<i>VOF</i>	= Volume-of-Fluid
ϵ	= ratio of results for a refinement level
θ	= Contact angle
σ	= Surface Tension Coefficient
ϕ	= Overall pore fraction of TBC
τ	= Geometric Factor based on TBC
ρ	= density
μs	= microseconds

II. Introduction

THE intake of Calcium-Magnesium-Alumino-Silicate (CMAS) particles by airplane engines poses a threat to the safety and durability of aircraft. For instance, in 1982, all four engines of a Boeing 747 on British Airways Flight 9 failed when the plane flew through a volcanic ash cloud made up of CMAS. When CMAS particles enter the engine, they melt due to the high temperatures and then solidify again on cooling lines [1]. This can cause damage to compressor blades and thermal barrier coatings, leading to overheating and engine stall [1]. Helicopters operating in sandy desert environments are at an even higher risk of CMAS damage [2]. The financial impact of CMAS ingestion can also be significant, as demonstrated by the closure of European airspace for six days following the eruption of Eyjafjallajökull in Iceland, which cost commercial airlines an estimated \$1.7 billion [3]. It is crucial to understand how CMAS behaves inside aircraft engines to prevent damage to both airplanes and the global economy.

Thermal Barrier Coatings (TBCs) are ceramic layers applied to aircraft engine components, such as high-pressure turbine blades, to protect them from prolonged exposure to heat [4]. These coatings can reduce component temperatures from 1700 K to around 1200 K [5]. As higher temperature turbines are required for high thrust applications, it is essential to continue developing and understanding coatings that can more effectively reduce heat transfer in engines. TBC systems can be made using various materials and methods. One approach is to use EB-PVD 7YSZ-based coatings, which have better aerodynamic performance and strain compliance than APS TBCs in the top coat, the layer most susceptible to CMAS infiltration [6]. The columnar microstructure of an EB-PVD coating is shown in Fig. 1, which shows both 'normal' and 'feathery' TBCs, and various stages between.

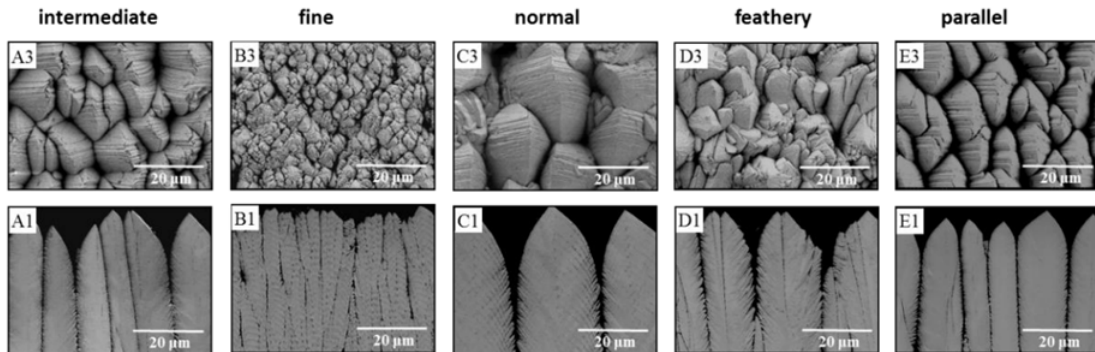


Fig. 1 Various morphologies of EB-PVD TBCs under magnification [6]. The top panel depicts the TBC surface, while the lower panel shows a side view from a cut TBC.

Melted CMAS infiltrates the inter-columnar gaps, and as the CMAS solidifies when the engine is not in use, the thermal expansion causes deformation in the TBC microstructure, which causes the desirable thermal insulation properties to degrade. The CMAS attack also causes a sintering phenomena to occur, which also erodes TBCs [7]. As manufacturers seek to help aero-engines achieve higher temperatures for efficiency gains, molten CMAS is becoming more of a problem [8]. Depending on composition, most forms of CMAS melt between 1150 - 1250 °C [9–12]. The sintering occurs when the molten CMAS comes into contact with the TBC. In one such case, molten volcanic ash interacted with a YSZ TBC to form yttria iron garnet [13].

Current literature has explored several important aspects of CMAS interaction with aircraft engines. One such study includes a computational model exploring CMAS particle fan-blade interaction [14]. This study found a distribution of particle sizes that are likely to move past the fan stage in aeroengines [14]. Another important study investigated how the impact of CMAS particle size and chemical composition would affect the particle's time to equilibrate on the nozzle guide vane. The particle's properties were summarized using the thermal Stokes number. The ratio of particle impact temperature ($T_{p,imp}$) to the temperature of the fluid (T_f) was measured. The study showed that the temperature of particles with a St_{th} below unity equilibrate with the temperature of the surrounding fluid in a fraction of the surrounding fluid's response time. St_{th} larger than unity led to particles that take much longer than the surrounding fluid's response time to equilibrate with the surrounding fluid [15]. This correlation was used as a validation methodology for this method [16]. This work seeks to do the following: 1) Give an overview of necessary background information to understand the processes involved in simulating CMAS, 2) Provide details of a methodology in which CMAS infiltration into a TBC is directly resolved 3) Perform a design study on a parameterized TBC model to understand which dimensions lead to desirable infiltration properties, such as longer infiltration times, or less heat transfer to the TBC. Literature has proposed the use of analytical models to describe the infiltration of CMAS. In these models, the flow of CMAS is said to be analogous to open, and concentric pipe flow, with modifying factors based on properties of the TBC [17].

However, the flow could also be considered a capillary-driven flow. Here, models such as Waghmare and Mitra's [18–20] look at flow in a rectangular microchannel. Accounting for geometric differences, this model could serve as an analytical basis for CMAS infiltration in a TBC.

Shortcomings of this analytical model, including heat transfer analysis and thermal expansion processes, can be accounted for via simulation.

This paper proposes the use of a finite-volume method (more specifically, the Eulerian Volume-of-Fluid Method), to resolve the infiltration of CMAS into an idealized TBC. Previous simulation-based infiltration models have used a FEM approach [5], but this approach comes with several challenges, including difficulties with resolving surface tension forces. Overall, the approach has the potential to push the understanding of infiltration processes. Previous work using this methodology has determined that experimental measurements for viscosity led to more accurate infiltration times. However, there was a large discrepancy between simulated and experimental infiltration times. This work seeks to further understand that discrepancy, and account for it in the simulation.

III. Methodology

The simulation methodology is explained in previous work [16, 21] and will be summarized here. The first step in simulating the infiltration of CMAS was to ensure the VOF method is a valid approach for capturing the melting-solidification of a CMAS particle. A mesh independence study was conducted in previous work [16], and it is shown that melting particles between the solidus and liquidus temperatures of CMAS can be accurately resolved with the VOF method. For multiphase physics, the Eulerian Multiphase Volume-of-Fluid method was used to simulate the interactions between the two Eulerian phases, air, and CMAS. Modeling surface tension properly is critical as the infiltration is driven mostly by capillary forces. The governing equations for the VOF method in Star-CCM+ ver. 18.02.008-R8 [22] are shown in a finite-volume formulation and include the the Conservation of Mass,

$$\frac{\partial}{\partial t} \int_V \rho dV + \oint_A v \bullet dA = \int_V (S) dV, \quad S = \sum_i S_{a_i} \rho_i \quad (1)$$

,the Conservation of Momentum,

$$\frac{\partial}{\partial t} \int_V \rho v dV + \oint_A \rho v \times v \bullet dA = \oint_A \rho I \bullet dA + \oint_A T \bullet dA + \int_V \rho g dV + \int_V f_b dV - \sum_i \int_A a_i \rho_i v_{d,i} \times v_{d,i} dA \quad (2)$$

and the Conservation of Energy,

$$\frac{\partial}{\partial t} \int_V \rho E dV + \oint_A [\rho Hv + p + a_i \rho_i H_i v_{d,i}] \bullet dA = - \oint_A \dot{q}'' \bullet dA + \oint_A T \bullet v dA + \int_V S_E dV + \int_V f_b dV. \quad (3)$$

Equations 3-5 couple to the Eulerian Multiphase VOF Transport Equation which is formulated as follows

$$\frac{\partial}{\partial t} \int_V a_i dV + \text{int}_A a_i v \bullet dA = \int_V \left(S_{a_i} - \frac{a_i}{\rho_i} \frac{D\rho_i}{Dt} \right) dV - \int_V \frac{1}{\rho_i} \nabla \bullet (a_i \rho_i v_{d,i}) dV \quad (4)$$

In these equations, the subscript i denotes a particular phase (in this case, air or CMAS), $a_i = V_i/V$ is the volume fraction of a particular phase, and S_{a_i} is a source term defined by the initialization of the phases. The VOF method implements a technique called High-Resolution Interface Capturing (HRIC). HRIC imposes a Courant number limit (i.e. $\text{Co} = 1.0$), and if the Courant number is exceeded, then the HRIC scheme reverts back to a standard upwind scheme, which results in a smeared interface. This smeared interface can be corrected by implementing temporal subcycling. The general idea of temporal subcycling is shown in Equation 5, where the right-hand side of the equation is a single source term that combines the right-hand side contributions from Equation 4.

$$\alpha^{n+\Delta t} V - \alpha^n V + \int_{t^n}^{t^{n+\Delta t}} \left(\sum_A \alpha_f(s) v \cdot da \right) = \int_{t^n}^{t^{n+\Delta t}} (S(\alpha(s), \dots)) ds \quad (5)$$

In this work, an implicit multi-stepping version of this temporal subcycling is employed, which gives an unconditionally stable solution, and a sharp interface is achieved if $\frac{CFL}{N_{imp}} \leq 0.5$. The sub-iterations calculated with Equation 6 are summed up to get the overall contribution for the whole time step.

$$\alpha_{i+1} V - \alpha_i V + \tau \left(\sum_A \alpha_{f,i+1}(\tau) v \cdot da \right) = \tau (S(\alpha^{n+\Delta t}, \dots)) \text{ for } i = 1, 2, \dots, N \quad (6)$$

A drawback of using the VOF method for the infiltration is the very small time steps required to resolve the CMAS infiltration. So, adaptive time-stepping combined with sub-iterations was used to balance computational speed and accuracy. A free-surface condition was enforced so that the Courant number ($\text{Co} = \frac{u\Delta t}{\Delta x}$) at the interface was around 1.0. Such a criterion is often demanded to limit the interfacial motion to only a cell. The VOF method requires the use of a segregated solver (i.e. the energy equation is solved in a separate system of equations). This solver is second-order accurate in space, and first-order accurate in time. However, the lower-order time accuracy is offset by the implicit multi-stepping in the segregated VOF solver, described in Equations 5 - 6.

The preliminary model was set up as a 2D geometry, a depiction of which is shown in Fig. 2. Where the feathery pattern shown on the left is repeated downward until the TBC column is $200 \mu\text{m}$ deep. This is half the size of a typical TBC column. The mesh is an unstructured trimmer mesh. The effect of contact angle was captured using prism layers at the wall. Boundary conditions, and domain dimensions, are summarized in Fig. 3 and Table 1. The top of the domain is a velocity inlet, and the bottom of the domain was set as a pressure outlet with a pressure smaller than the reference pressure. This pressure difference between the inlet and outlet was set up so that a pressure gradient pushes the CMAS particle downward. The sides of the domain are also set as pressure outlets. Conjugate heat transfer was considered by setting the TBC as a solid region, the walls of the TBC were prescribed a temperature gradient of $1 \text{ K}/\mu\text{m}$, such that the top of the coating is close to a typical operating temperature for an engine environment. The gradient is defined this way because a typical YSZ EB-PVD TBC is around $400 \mu\text{m}$ deep, and manages to be around 400 K cooler at the bottom of the TBC than the top, such that the operating temperature is below the melting point of the materials used. It should be noted there is only a gradient in the x-direction, so any walls on the same x-plane will have a constant temperature, and any walls along the same y-plane will have a temperature that varies.

The air phase was modeled as a constant-density fluid in this simulation. Thus, it is necessary to account for air getting trapped within the feather gaps as it would prevent the CMAS from infiltrating those gaps. To accomplish this, the interface between the fluid and solid regions was set as a porous boundary, only allowing air to escape. The rate at which air was allowed to escape was based on a user-defined external pressure, inertial resistance, and viscous resistance, which were 0 Pa (reference), 100 (dimensionless), and 1 m/s respectively. Hence, the air can escape the fluid domain at a maximum velocity of 0.01 m/s according to Eq. 7 [22].

$$\Delta P = -\rho(\alpha|v_n| + \beta)v_n \quad (7)$$

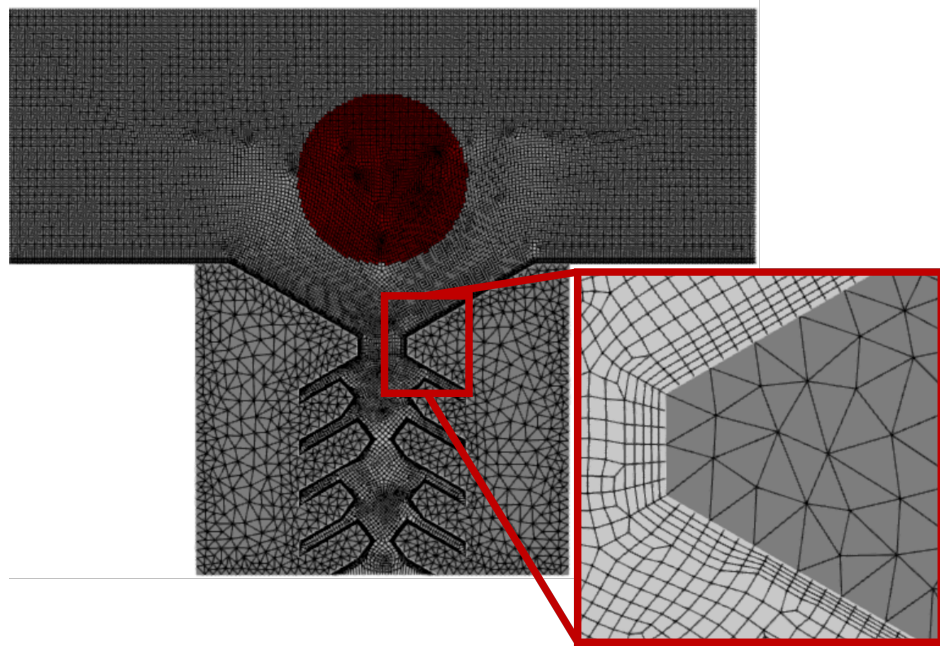


Fig. 2 Zoomed out mesh, and mesh zoomed in around wall region

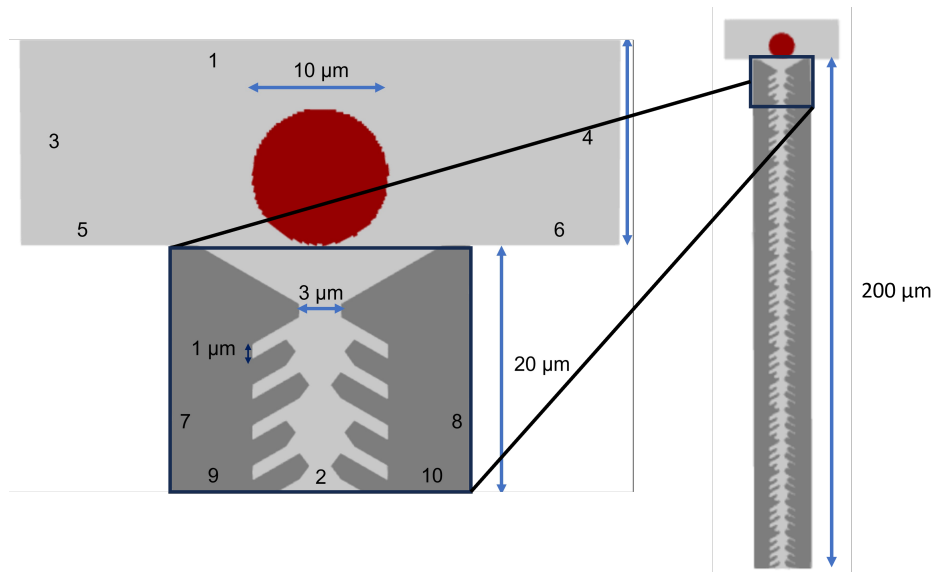


Fig. 3 Geometry with labeled dimensions and boundary conditions

Table 1 Summary of Labaled Boundary Conditions (Pressure values with respect to reference pressure)

Label	Boundary Condition	Value (Units)
1	Velocity	$0.1 \mu\text{m/s}$
-	$\frac{\partial T}{\partial x}$	$1 \text{ K}/\mu\text{m}$
2	Pressure	-25000 Pa
-	$\frac{\partial T}{\partial x}$	$1 \text{ K}/\mu\text{m}$
3-4	Pressure	10000 Pa
-	$\frac{\partial T}{\partial x}$	$1 \text{ K}/\mu\text{m}$
5-10	$\frac{\partial T}{\partial x}$	$1 \text{ K}/\mu\text{m}$

Table 2 Summary of thermal and physical properties of CMAS and TBC

Property	CMAS	TBC
Thermal Conductivity (W/m-K)	1.15 [25]	tabular [24]
Specific Heat (J/kg-K)	900 [26]	tabular [24]
Density (kg/m ³)	2690 [27]	4800 [28]
Dynamic Viscosity (Pa-s)	Polynomials w.r.t Temperature [5]	-
Latent Heat of Fusion (J/kg)	1.973×10^7 [9]	-
Surface Tension (N/m)	0.4 [29]	-

The 2D geometry and mesh can be seen in Fig 2. The preliminary results presented here will use this 2D formulation. The wall contact angle of the CMAS phase is expected to be somewhere between 40 and 60 degrees based on experiments [23]. These values are temperature dependent though. For simplicity, a constant wall contact angle of 40 degrees was chosen.

The thermal gradient described above for boundary conditions was also used as the initial condition for both the fluid region and solid region, except for the CMAS particle, which had a variable starting temperature. The fluid domain's initial velocity was set such that there was a very small downward velocity. This is done because it helps with convergence in the first calculations in the simulation. The CMAS particle was set at 0.2 m/s downward to ensure a quick interaction with the TBC. The reference pressure is 1 atm. While it could potentially make more sense to use engine operating pressures for the simulation's reference pressure, this domain was set up to be more in line with experiments conducted by Naraparaju et al. [10, 17, 23] to ensure the comparison to experimental data is as accurate as possible. Gravity was also enabled to capture any infiltration effects from buoyancy. Turning on gravity also adds the Boussinesq Approximation to the energy equation to account for natural convection. However, the effects of natural convection are low due to the small domain size.

Properties of both the CMAS and the TBC can affect the infiltration. Some of these properties are widely documented, such as thermal conductivity of the TBC [24]. Table 2 shows the properties for both the CMAS and the TBC used in these simulations. Blank entries are properties not required by the models selected (in this case, for the solid TBC region).

One important departure from previous work, however, is the use of the melting-solidification flow stop model to achieve a more accurate infiltration time. It is proposed that varying the flowability threshold for the solid CMAS can bring the solution more in line with the experimental infiltration results.

IV. Preliminary Results

A. Mesh Sensitivity Study

Mesh sensitivity was conducted based on the infiltration depth at 0.1 s of physical time. This parameter was chosen because it is a parameter for which experimental data exists, and is therefore important for validation in this study. The physical time to extract the infiltration depth was chosen because beyond that time, error accumulates in the simulation,

Table 3 Table with Mesh Sensitivity Results from Figure 5

Representative Mesh Size (m)	Infiltration depth at 0.1 s (m)
2.1×10^{-7}	4.465663e-05
1.4×10^{-7}	3.280286e-05
1.0×10^{-7}	3.233177e-05
7.5×10^{-8}	3.238081e-05

causing the mass of CMAS to grow beyond the initial value, causing the result to be non-physical. This non-physical phenomenon can be seen in the coarsest mesh in Figure 4a, and the result becomes more clear in Figure 4b - 4d. The results in Figure 5 and Table 3 show asymptotic convergence. With such incredibly small variations with coarser mesh sizes, a mesh with a base size of 1.4×10^{-7} m will be used for further simulations. Performing the formal grid convergence index (GCI) calculations [30, 31] shows that the results in Table 3 mean this is monotonically converging, because $0 < \epsilon_{21}/\epsilon_{32} = 0.004 < 1$, and a GCI of 7.5×10^{-4} .

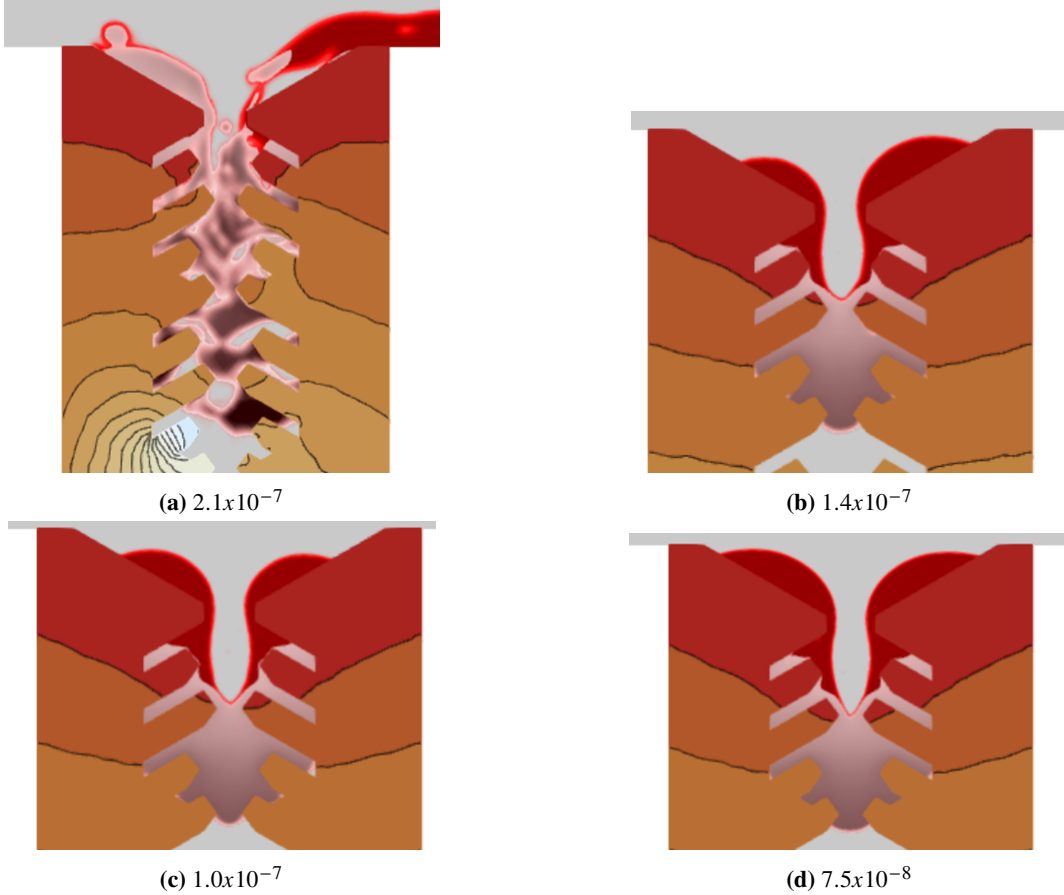


Fig. 4 CMAS Infiltration at different levels of mesh refinement

B. Analytical Benchmark

Experimental results in Figure 6 for infiltration depth v. time are compared to simulations. These experimental results come from the German Aerospace Center, and the material used for “CMAS 1” is consistent with the material defined in the simulation. Unfortunately, the data is much farther advanced in time and with much less time resolution than the simulation. Numerical errors in mass conservation in the simulation tend to add up to a point where the result is

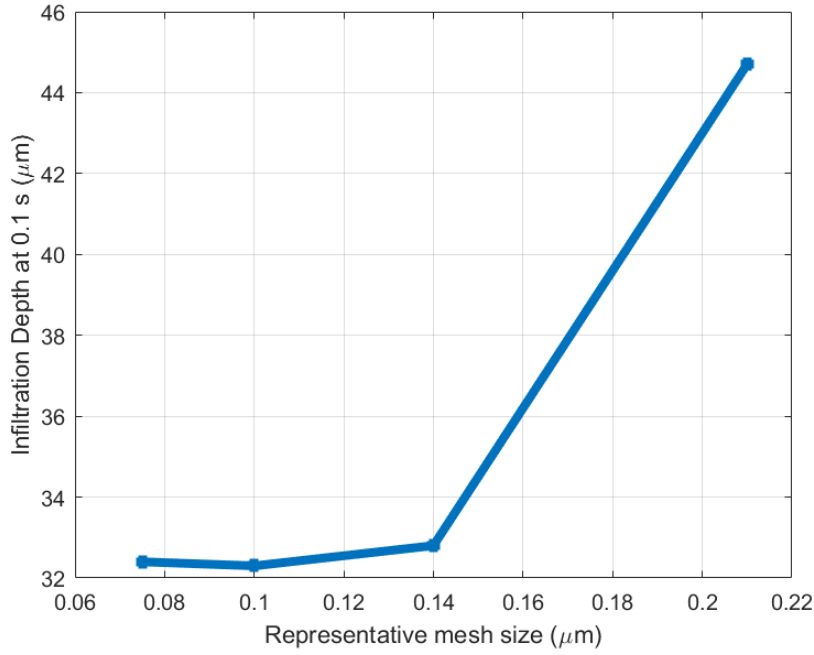


Fig. 5 Infiltration Depth (m) as a function of representative mesh size (m

non-physical around 0.5 s, making it difficult to compare to any time points in Figure 6. So instead, the simulation data will be compared to the open-pipe and concentric pipe models described in Naraparaju et. al. [23]. The formulations for this model can be seen below.

$$t = \frac{\mu r h^2}{2\sigma k \cos\theta} \quad (8)$$

here, t is the infiltration time, r is the radius open for infiltration, h is the infiltration depth, μ, σ, θ are viscosity, surface tension, and contact angle respectively [17, 32]. The parameter k represents the porosity and varies depending on whether the open-pipe or concentric-pipe model is being used. Some difficulties arise here, as some of the properties in the above equation vary nonlinearly with temperature, so initial values will be used for the calculations. The open-pipe model defines k as the following

$$k_o = \frac{r^2 \phi^2}{8\tau (1 - \phi)^2} \quad (9)$$

here ϕ is the overall pore fraction, and τ is a geometric factor based on a ratio of area of the column to area of the feather arms, and it was found to be 2.31 for feathery microstructures [23]. The concentric pipe model is similar, but defines k as

$$k_o = \frac{\phi}{8\tau^2} b^2 \left[1 + \frac{a^2}{b^2} + \left(1 - \frac{a^2}{b^2} \right) \frac{1}{\ln(a/b)} \right] \quad (10)$$

where a and b are the outer radii of the concentric pipes [23]. The results of the benchmark to the analytical models are shown in Figure 7. While the simulation under-predicts depth compared to the models, it is important to note that these are of the same order of magnitude, which supports the idea of neglecting chemical interactions in future simulations, as they may not be first-order contributors to the infiltration process.

C. Characterization Based on Viscosity

In this study, two different formulations of the CMAS dynamic viscosity were evaluated: the GRD viscosity model [33], and experimental viscosity measurements [23]. The difference between the experimental and GRD viscosity is shown in Fig. 8, where the experimental viscosity is higher throughout the entire temperature range. Simulations were

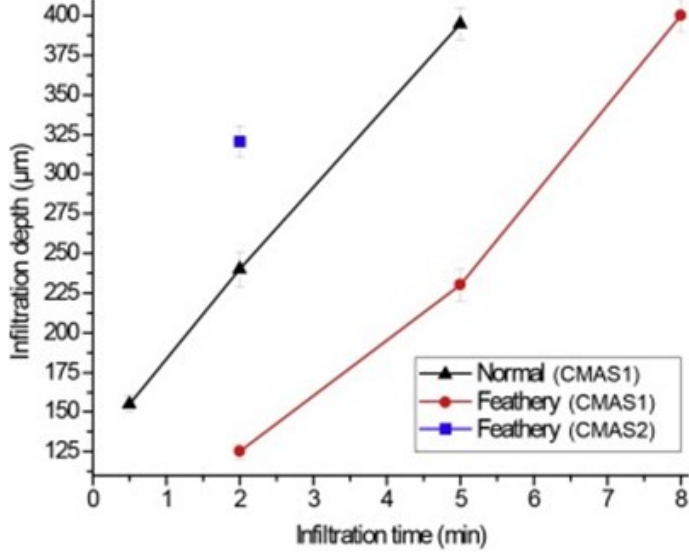


Fig. 6 Experimental Infiltration Depth v. Time Measurements

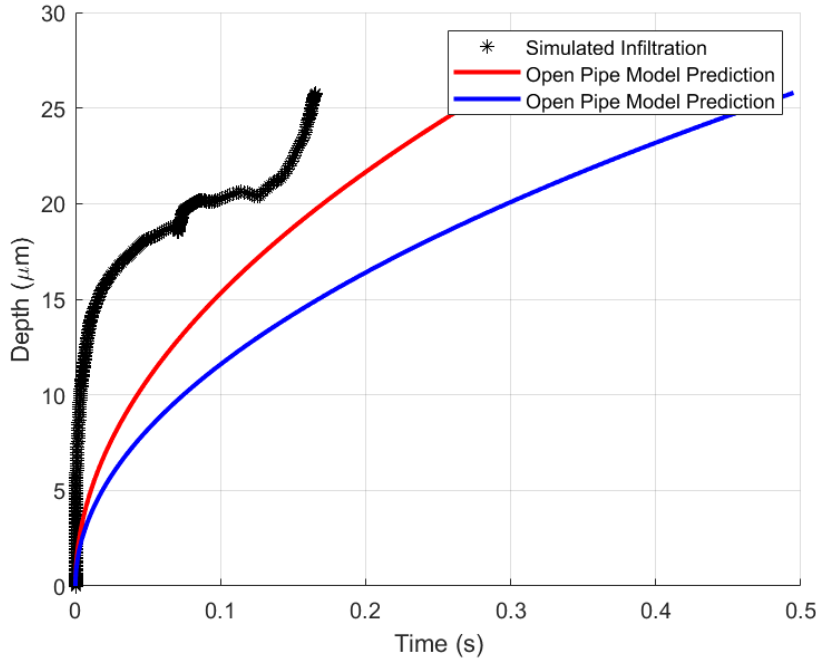


Fig. 7 Comparison of Simulation Results to Analytical Models for infiltration depth

run with both the experimental and GRD viscosity, using a temperature-based polynomial to approximate the data. Figure 9 shows that the infiltration time for the experimental viscosity is around 2.5x slower as the GRD viscosity. However, the infiltration times measured here are several orders of magnitude faster than those measured in experiments [23] if the infiltration rate curves are extrapolated out to the experimental TBC depth [34].

Computational results from other work show a larger difference between the experimental and numerical infiltration times [5]. However, those results treated both the experimental and GRD viscosity as constant values of 6, and 0.6 Pa-s respectively. Those results also did not account for conjugate heat transfer effects or the existence of air in the domain (i.e. no surface tension effects). So it makes sense that the results presented here would show overall longer infiltration

times. The results presented in this section also do not account for any melting-solidification processes and have the same starting temperature such that the particle is fully-liquid throughout the simulation. An image of how the viscosity varies with temperature throughout the domain is shown in Fig. 10.

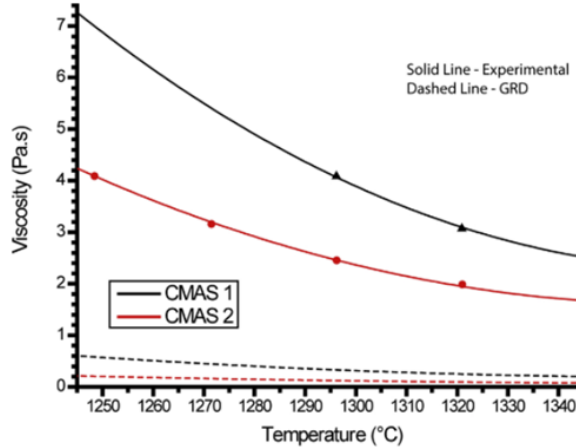


Fig. 8 Experimental v. GRD Viscosity Curves

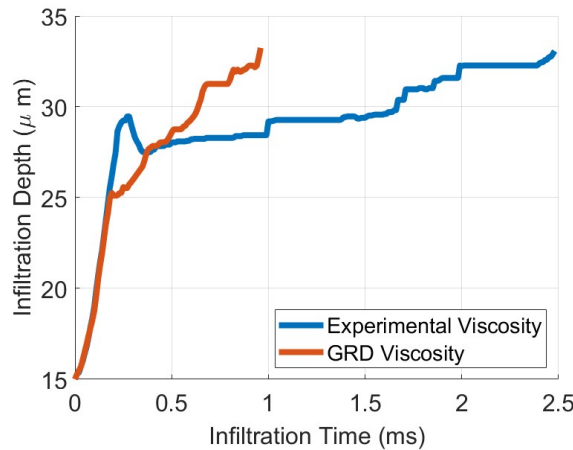


Fig. 9 Experimental v. GRD Infiltration Time

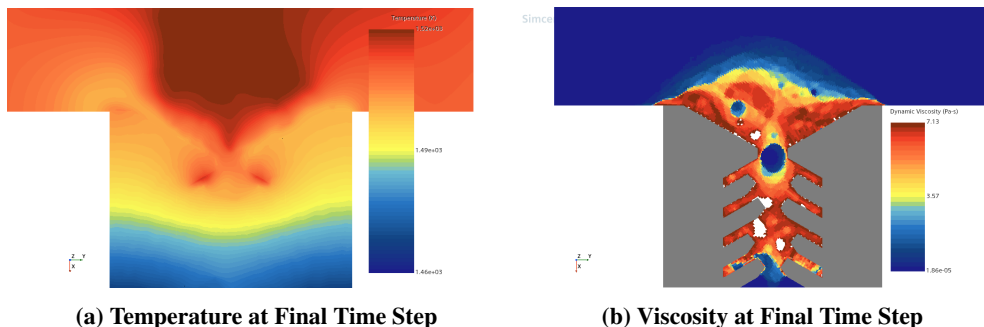


Fig. 10 Viscosity Variation with Temperature in Domain

D. Expected Results

Results from Naraparju et. al. [23] show that the concentric pipe model has a shorter infiltration depth than their experimental results at a given time, and the open pipe model has a farther infiltration depth than the experiments. This information is summarized in 4. If the simulation data from 7 is cleaned up and extrapolated with a base-10 logarithmic curve fit, a depth can be estimated for the simulation at the same time as the experiment. However, this result shows a much shorter infiltration depth than both analytical models and the experiment. It is expected that this result will change once the simulation is refined to handle longer runtimes. The result will also be refined by finding a more robust extrapolation method.

Table 4 Comparison of infiltration depth (μm) at 120 s of infiltration time for experiments and analytical models

Result	Depth at 120 s (μm)
Experimental Measurement	125
Concentric Pipe Model	95
Open Pipe Model	176
Extrapolated Simulation	38

References

- [1] Chen, W., and Zhao, L., “Review – Volcanic Ash and its Influence on Aircraft Engine Components,” *Procedia Engineering*, Vol. 99, 2015, pp. 795–803. <https://doi.org/10.1016/j.proeng.2014.12.604>.
- [2] Smialek, J. L., “The Chemistry of Saudi Arabian Sand: A Deposition Problem on Helicopter Turbine Airfoils NASA THE CHEMISTRY OF SAUDI ARABIAN SAND: A DEPOSITION PROBLEM ON HELICOPTER TURBINE AIRFOILS,” , 1991.
- [3] Schechter, O., Apr 2010. URL <https://web.archive.org/web/20100419004949/http://blog.newsweek.com/blogs/thehumancondition/archive/2010/04/16/smoked-out-why-volcanic-ash-and-planes-fight-for-the-same-small-air-space.aspx>.
- [4] Bennett, T. D., and Yu, F., “A nondestructive technique for determining thermal properties of thermal barrier coatings,” *Journal of Applied Physics*, Vol. 97, 2005, p. 13520. <https://doi.org/10.1063/1.1826217>, URL <https://aip.scitation.org/doi/abs/10.1063/1.1826217>.
- [5] Sirigiri, A. K., and Kowalczyk, P. D.-I. W., “Modeling and simulation of CMAS infiltration in EB-PVD TBCs,” , 2018.
- [6] Flores Renteria, A., and W.A.Kaysser, “A small-angle scattering analysis of the influence of manufacture and thermal induced morphological changes on the thermal conductivity of EB-PVD PYSZ thermal barrier coatings,” *Fakultät für Georesourcen und Materialtechnik*, 2007.
- [7] Peng, H., Wang, L., Guo, L., Miao, W., Guo, H., and Gong, S., “Degradation of EB-PVD thermal barrier coatings caused by CMAS deposits,” *Progress in Natural Science: Materials International*, Vol. 22, No. 5, 2012, pp. 461–467. <https://doi.org/https://doi.org/10.1016/j.pnsc.2012.06.007>, URL <https://www.sciencedirect.com/science/article/pii/S100200711200086X>.
- [8] Boyce, M. P., 2 - *Advanced industrial gas turbines for power generation*, Woodhead Publishing, 2012, pp. 44–102. <https://doi.org/10.1533/9780857096180.44>, URL <https://www.sciencedirect.com/science/article/pii/B978085709013350002X>.
- [9] Costa, G., Harder, B. J., Wiesner, V. L., Zhu, D., Bansal, N., Lee, K. N., Jacobson, N. S., Kapush, D., Ushakov, S. V., and Navrotsky, A., “Thermodynamics of reaction between gas-turbine ceramic coatings and ingested CMAS corrodents,” *Journal of the American Ceramic Society*, Vol. 102, No. 5, 2019, pp. 2948–2964. <https://doi.org/https://doi.org/10.1111/jace.16113>, URL <https://ceramics.onlinelibrary.wiley.com/doi/abs/10.1111/jace.16113>.
- [10] Naraparaju, R., Schulz, U., Mechnick, P., Döbber, P., and Seidel, F., “Degradation study of 7wt.% yttria stabilised zirconia (7YSZ) thermal barrier coatings on aero-engine combustion chamber parts due to infiltration by different CaO–MgO–Al₂O₃–SiO₂ variants,” *Surface and Coatings Technology*, Vol. 260, 2014, pp. 73–81. <https://doi.org/https://doi.org/10.1016/j.surfcoat.2014.08.079>.
- [11] Wellman, R., Whitman, G., and Nicholls, J. R., “CMAS corrosion of EB PVD TBCs: Identifying the minimum level to initiate damage,” *International Journal of Refractory Metals and Hard Materials*, Vol. 28, No. 1, 2010, pp. 124–132. <https://doi.org/https://doi.org/10.1016/j.ijrmhm.2009.07.005>, URL <https://www.sciencedirect.com/science/article/pii/S0263436809001073>.
- [12] Krämer, S., Yang, J., Levi, C. G., and Johnson, C. A., “Thermochemical Interaction of Thermal Barrier Coatings with Molten CaO–MgO–Al₂O₃–SiO₂ (CMAS) Deposits,” *Journal of the American Ceramic Society*, Vol. 89, No. 10, 2006, pp. 3167–3175. <https://doi.org/https://doi.org/10.1111/j.1551-2916.2006.01209.x>, URL <https://ceramics.onlinelibrary.wiley.com/doi/abs/10.1111/j.1551-2916.2006.01209.x>.
- [13] Xia, J., Yang, L., Wu, R. T., Zhou, Y. C., Zhang, L., Huo, K. L., and Gan, M., “Degradation mechanisms of air plasma sprayed free-standing yttria-stabilized zirconia thermal barrier coatings exposed to volcanic ash,” *Applied Surface Science*, Vol. 481, 2019, pp. 860–871. <https://doi.org/https://doi.org/10.1016/j.apsusc.2019.03.084>, URL <https://www.sciencedirect.com/science/article/pii/S0169433219307044>.
- [14] Vogel, A., Durant, A., Cassiani, M., Clarkson, R., Slaby, M., Diplas, S., Krüger, K., and Stohl, A., “Simulation of Volcanic Ash Ingestion Into a Large Aero Engine: Particle–Fan Interactions,” *Journal of Turbomachinery*, Vol. 141, 2018. <https://doi.org/10.1115/1.4041464>.
- [15] Bojdo, N., and Filippone, A., “A Simple Model to Assess the Role of Dust Composition and Size on Deposition in Rotorcraft Engines,” *Aerospace*, Vol. 6, No. 4, 2019, p. 44. URL <https://www.mdpi.com/2226-4310/6/4/44>.
- [16] Cavainolo, B., and Kinzel, M., “Investigation of Volume-of-Fluid Method to Simulate Melting–Solidification of CMAS Particles,” *ASME 2022 Fluids Engineering Division Summer Meeting*, Vol. Volume 2: Multiphase Flow (MFTC); Computational Fluid Dynamics (CFDTC); Micro and Nano Fluid Dynamics (MNFDTC), V002T04A002, 2022. <https://doi.org/10.1115/fedsm2022-85863>, URL <https://doi.org/10.1115/FEDSM2022-85863>.

- [17] Naraparaju, R., Hüttermann, M., Schulz, U., and Mechnich, P., “Tailoring the EB-PVD columnar microstructure to mitigate the infiltration of CMAS in 7YSZ thermal barrier coatings,” *Journal of the European Ceramic Society*, Vol. 37, No. 1, 2017, pp. 261–270. [https://doi.org/https://doi.org/10.1016/j.jeurceramsoc.2016.07.027](https://doi.org/10.1016/j.jeurceramsoc.2016.07.027), URL <https://www.sciencedirect.com/science/article/pii/S0955221916304058>.
- [18] Waghmare, P. R., and Mitra, S. K., “On the Derivation of Pressure Field Distribution at the Entrance of a Rectangular Capillary,” *Journal of Fluids Engineering*, Vol. 132, No. 5, 2010, p. 054502. <https://doi.org/10.1115/1.4001641>, URL <https://doi.org/10.1115/1.4001641>.
- [19] Waghmare, P. R., and Mitra, S. K., “Modeling of combined electroosmotic and capillary flow in microchannels,” *Analytica Chimica Acta*, Vol. 663, No. 2, 2010, pp. 117–126. [https://doi.org/https://doi.org/10.1016/j.aca.2010.01.055](https://doi.org/10.1016/j.aca.2010.01.055), URL <https://www.sciencedirect.com/science/article/pii/S0003267010001571>.
- [20] Waghmare, P. R., and Mitra, S. K., “Finite reservoir effect on capillary flow of microbead suspension in rectangular microchannels,” *Journal of Colloid and Interface Science*, Vol. 351, No. 2, 2010, pp. 561–569. [https://doi.org/https://doi.org/10.1016/j.jcis.2010.08.039](https://doi.org/10.1016/j.jcis.2010.08.039), URL <https://www.sciencedirect.com/science/article/pii/S0021979710009343>.
- [21] Cavainolo, B. A., Kinzel, M. P., Naraparaju, R., and Kabir, M. R., “Simulating CMAS Infiltration of an EB-PVD Thermal Barrier Coating Using the Volume-of-Fluid Method,” , 2023.
- [22] Siemens, “STAR-CCM+ User’s Manual,” , 2023.
- [23] Naraparaju, R., Gomez Chavez, J. J., Niemeyer, P., Hess, K.-U., Song, W., Dingwell, D. B., Lokachari, S., Ramana, C. V., and Schulz, U., “Estimation of CMAS infiltration depth in EB-PVD TBCs: A new constraint model supported with experimental approach,” *Journal of the European Ceramic Society*, Vol. 39, No. 9, 2019, pp. 2936–2945. [https://doi.org/https://doi.org/10.1016/j.jeurceramsoc.2019.02.040](https://doi.org/10.1016/j.jeurceramsoc.2019.02.040), URL <https://www.sciencedirect.com/science/article/pii/S0955221919301335>.
- [24] Han, J., Zou, Y., Wu, D., and Zhang, Y., “Investigating the thermal, mechanical and thermal cyclic properties of plasma-sprayed Al₂O₃-7YSZ/7YSZ double ceramic layer TBCs,” *Journal of the European Ceramic Society*, Vol. 43, No. 9, 2023, pp. 4124–4135. <https://doi.org/https://doi.org/10.1016/j.jeurceramsoc.2023.03.004>, URL <https://www.sciencedirect.com/science/article/pii/S095522192300184X>.
- [25] Bakal, A., Roebbecke, K., Wang, H., Deng, W., Zhang, X., and Fergus, J. W., *Evolution of the Thermal Conductivity of Sm₂Zr₂O₇ Under CMAS Attack*, Springer International Publishing, Cham, 2017, pp. 227–235. https://doi.org/10.1007/978-3-319-52333-0_21, URL https://doi.org/10.1007/978-3-319-52333-0_21.
- [26] Kakuda, T. R., Levi, C. G., and Bennett, T. D., “The thermal behavior of CMAS-infiltrated thermal barrier coatings,” *Surface and Coatings Technology*, Vol. 272, 2015, pp. 350–356. <https://doi.org/https://doi.org/10.1016/j.surfcoat.2015.03.043>, URL <https://www.sciencedirect.com/science/article/pii/S0257897215002819>.
- [27] Bansal, N. P., and Choi, S. R., “Properties of CMAS glass from desert sand,” *Ceramics International*, Vol. 41, No. 3, Part A, 2015, pp. 3901–3909. <https://doi.org/https://doi.org/10.1016/j.ceramint.2014.11.072>, URL <https://www.sciencedirect.com/science/article/pii/S027288421401832X>.
- [28] Kakuda, T. R., Limarga, A. M., Bennett, T. D., and Clarke, D. R., “Evolution of thermal properties of EB-PVD 7YSZ thermal barrier coatings with thermal cycling,” *Acta Materialia*, Vol. 57, No. 8, 2009, pp. 2583–2591. <https://doi.org/https://doi.org/10.1016/j.actamat.2009.02.019>, URL <https://www.sciencedirect.com/science/article/pii/S1359645409001013>.
- [29] Bravo, L. G., Jain, N., Khare, P., Murugan, M., Ghoshal, A., and Flatau, A., “Physical aspects of CMAS particle dynamics and deposition in turboshaft engines,” *Journal of Materials Research*, Vol. 35, No. 17, 2020, pp. 2249–2259. <https://doi.org/10.1557/jmr.2020.234>, URL <https://doi.org/10.1557/jmr.2020.234>.
- [30] Eça, L., and Hoekstra, M., “A procedure for the estimation of the numerical uncertainty of CFD calculations based on grid refinement studies,” *Journal of Computational Physics*, Vol. 262, 2014, pp. 104–130. <https://doi.org/https://doi.org/10.1016/j.jcp.2014.01.006>, URL <https://www.sciencedirect.com/science/article/pii/S0021999114000278>.
- [31] Celik, I. B., Ghia, U., Roache, P. J., and Freitas, C. J., “Procedure for estimation and reporting of uncertainty due to discretization in CFD applications,” *Journal of fluids Engineering-Transactions of the ASME*, Vol. 130, No. 7, 2008.
- [32] Zhao, H., Levi, C. G., and Wadley, H. N., “Molten silicate interactions with thermal barrier coatings,” *Surface and Coatings Technology*, Vol. 251, 2014, pp. 74–86. <https://doi.org/https://doi.org/10.1016/j.surfcoat.2014.04.007>, URL <https://www.sciencedirect.com/science/article/pii/S0257897214002977>.

- [33] Giordano, D., Russell, J. K., and Dingwell, D. B., “Viscosity of magmatic liquids: A model,” *Earth and Planetary Science Letters*, Vol. 271, No. 1, 2008, pp. 123–134. [https://doi.org/https://doi.org/10.1016/j.epsl.2008.03.038](https://doi.org/10.1016/j.epsl.2008.03.038), URL <https://www.sciencedirect.com/science/article/pii/S0012821X08002240>.
- [34] Stein, Z., Cavainolo, B., Tetard, L., Kinzel, M. P., Naraparaju, R., Schulz, U., and Raghavan, S., *CMAS Infiltration and Mitigation Strategies for Minimizing Premature Degradation Failure of High Temperature Ceramic Coatings in Turbine Engines*, 2023. <https://doi.org/10.2514/6.2023-0179>, URL <https://arc.aiaa.org/doi/abs/10.2514/6.2023-0179>.